

# Hardware Demonstration of Atomic Force Microscopy Imaging via Compressive Sensing and $\mu$ -path Scans

Roger A. Braker<sup>1</sup>, Yufan Luo<sup>2</sup>, Lucy Y. Pao<sup>1</sup>, and Sean B. Andersson<sup>2,3</sup>

<sup>1</sup>Dept. of Electrical, Computer, and Energy Engineering, University of Colorado, Boulder, CO, 80309

<sup>2</sup>Division of Systems Engineering, <sup>3</sup> Dept. of Mechanical Engineering, Boston University, Boston, MA 02215  
{roger.braker,pao}@colorado.edu, {luoyuf,sanderss}@bu.edu

**Abstract**—In this paper we describe an implementation of non-raster scanning of atomic force microscopy images where randomly placed short scans are combined with compressive-sensing based image reconstruction algorithms to produce the final image. We describe implementation details and compare the achievable imaging rate and image quality to raster-scanned images. Our experimental results show improvements of up to approximately a five times reduction in scanning time while revealing several practical challenges.

## I. INTRODUCTION

The Atomic Force Microscope (AFM) is a nano-scale imaging instrument which acquires an image of the surface topography of a sample by interrogating it with an atomically-sharp probe. While there are a variety of imaging modes, the fundamental effect is that as the probe is brought to the sample, the inter-molecular forces between the probe and sample cause the probe to deflect. A controller is then wrapped around that deflection signal to maintain a constant level. The control output is then a measure of the sample topology [1].

Although the AFM has excellent spatial resolution, one key drawback is that the imaging process is slow—often on the order of minutes for commercially available instruments. This has led to a large research effort to increase the speed of AFMs. Most of these efforts focus on various methods to increase the overall speed of the system. Approaches include building stiff piezo stages with higher first-resonance frequencies (e.g., [2], [3]); replacing the standard triangle wave reference with a reference signal which has a more friendly harmonic content such as spirals or Lissajous patterns (e.g., [4]–[6]), or driving the stage with a pure sinusoid [7]; and using advanced control methods, including very effective use of feedforward control [8]–[11]. In the  $z$ -direction, the sample surface acts as an unknown disturbance, making feedforward approaches less effective. Here, improvements have been made with advanced feedback control techniques like  $H_\infty$  and high speed hardware such as fast piezo stacks [7], [12].

One of the drawbacks to these approaches is that to increase the actual imaging rate, all the pieces have to be improved in lockstep [13]. Increasing the speed of one element is of limited value because it will only expose

a bottleneck somewhere else. For example, increasing the bandwidth of the  $xy$ -stage leads to a bottleneck in the  $z$ -direction, and vice versa. Increasing either can expose deficiencies in the power amplifiers or the sample rate of the digital control system.

It is in this light that algorithmic approaches which seek to improve the imaging rate not by *moving faster* but rather by *sampling less* find their appeal. For a class of samples that can be described by planar curves, a method termed Local Circular Scanning (LCS) replaces the raster with a sequence of circular scans which track the sample edge and can reduce scanning time by an order of magnitude [14], [15].

Another vein which has received attention in the last few years aims to leverage the idea of undersampling [16]–[18]. Taking advantage of the redundancy in many interesting signals, this approach achieves increased imaging rates by reducing the number of pixels to be acquired while, unlike local techniques such as LCS, still producing full frame images. The final surface image is created from the measured pixels using signal processing and image reconstruction techniques, motivated in many cases by the theory of compressive sensing.

Perhaps the easiest scanning pattern for sub-sampling is to simply skip some of lines in the scan [19]. Existing non-raster scanning patterns such as spirals can also be applied for sub-sampling of images and have been demonstrated experimentally to produce faster imaging while still producing accurate reconstructions [16], [20]. However, from the theory of compressive sensing, it is known that randomized sampling is critical to producing accurate reconstructions for a broad class of samples. Thus, ideally, one would acquire a random collection of the pixels [17]. However, doing so requires the tip to be repeatedly lifted and re-engaged with the sample; each such engagement takes a significant amount of time. Inspired by this, we have previously introduced the notion of  $\mu$ -paths to balance randomness with continuous scanning [21]. In this paper, we give a hardware demonstration<sup>1</sup> of this approach [21].

## II. COMPRESSIVE SENSING VIA SHORT $\mu$ -PATH SCANS

Most real-world signals, including the images of nano-scale surface topography, are *sparse* or *compressible* when

This work was supported in part by the US NSF through CMMI-1234980, CMMI-1234845, and DBI-135272, by Agilent Technologies, Inc., and by a Fellowship from the Hanse-Wissenschaftskolleg, Delmenhorst, Germany.

<sup>1</sup>The software portion of the implementation described in this paper can be found at [https://github.com/rabraker/AFM\\_CS/](https://github.com/rabraker/AFM_CS/)

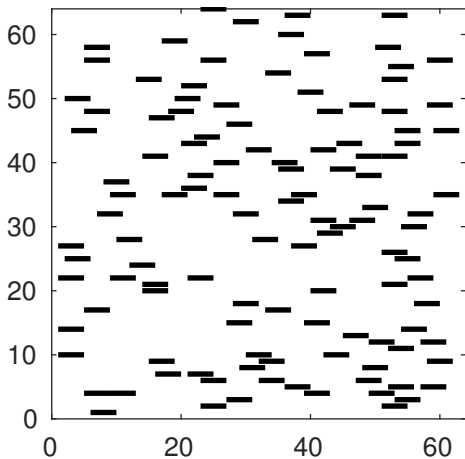


Fig. 1: An example of a  $\mu$ -path sampling pattern for a  $64 \times 64$  pixel image.

represented in an appropriate basis. Compressive Sensing (CS) is a signal processing technique for recovering undersampled sparse or compressible signals from a relatively small number of measurements [22].

CS methods seek the true image signal  $x \in \mathbb{R}^n$  from the following observation equation,

$$y = \Phi x = \Phi \Psi \eta, \quad (1)$$

where  $y \in \mathbb{R}^m$  is the observation vector,  $\Phi$  is an  $m \times n$  matrix defining the measurements,  $\Psi$  is an  $n \times n$  sparsity basis and  $\eta$  is the sparse representation of  $x$  in the domain of  $\Psi$ . In general,  $m \ll n$ . In the AFM application, the probe can only measure a single pixel at a time. As a result,  $\Phi$  is a sparse matrix with each row having only one nonzero entry. Thus,  $y$  is a subset of  $x$ .

In traditional CS, random sampling, such as selecting to sample each pixel with the same probability, is considered an effective sampling strategy for stable reconstruction. However, random sampling does not offer significantly lower data acquisition time for AFM, since the probe has to visit scattered sampling locations, lifting the probe tip after each measurement and reengaging it to the surface to acquire the next pixel. Paths that limit the need to repeatedly re-engage the tip are more desirable in practice. The  $\mu$ -path pattern, introduced in [21], uses small, linear scans, each beginning at randomly selected pixels (see, e.g. Fig. 1 for one such pattern). Scanning according to a  $\mu$ -path pattern involves moving the tip to the next starting pixel, engaging to the surface, scanning along a short path, lifting the tip, and repeating. This pattern aims to balance the need for random, independent sampling with continuous tip motion. Faithful recovery from  $\mu$ -path scans has previously been demonstrated through simulation [18], [23].

One common realization of the CS-based reconstruction problem, known as basis pursuit (BP), is given by the following optimization problem,

$$\text{minimize } \|\eta\|_1 \quad \text{subject to } y = \Phi \Psi \eta, \quad (2)$$

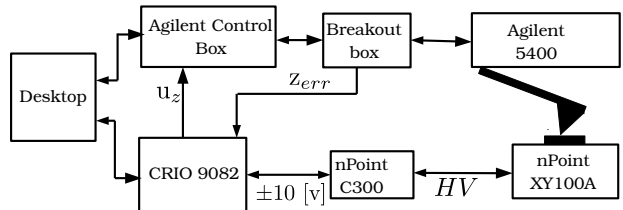


Fig. 2: Schematic depiction of the experimental setup

where  $\|\cdot\|_1$  is the  $l_1$  norm of the signal. While BP is a computationally demanding algorithm, particularly for large images, it does provide effective reconstructions. More efficient greedy algorithms have also been developed, including one by two of authors that was designed specifically for the sampling matrices in the AFM setting [23].

### III. EXPERIMENTAL SETUP

Our experimental setup, illustrated in Fig. 2, consists of an Agilent 5400 AFM retrofitted with an nPoint NPXY100A piezoelectric stage. Through a breakout box, the Agilent 5400 provides access to the  $z$ -axis deflection signal. When the Agilent software is set to open-loop mode, a  $\pm 10$  v input on the standard control box allows control of the  $z$ -axis piezo. The total range of the  $z$ -axis piezo is  $7 \mu\text{m}$ . The Agilent hardware does not provide access to the  $z$ -axis stepper motor used for the coarse engagement, so for the initial tip engagement to the sample, we use the standard Agilent software. Once the initial engagement is completed, we set the Agilent software to open-loop mode.

All control logic is programmed into a Xilinx LX150 Field Programmable Gate Array (FPGA) inside a cRIO-9082 from National Instruments. The cRIO includes modular 16 bit analog-to-digital and digital-to-analog modules. In this paper, all control is done at 25 kHz, a sampling rate chosen based on the identified system dynamics.

#### A. Control

The control laws used for all three axes are simple integral controllers of the form

$$\frac{U(q)}{E(q)} = D(q) = \frac{K_i q}{q-1}, \quad (3)$$

where, for example, for the  $x$ -axis,  $E(q) = X(q) - X_{ref}$ . The errors for the other axes are defined similarly. We use  $q$  as the discrete time Laplace operator to avoid confusion with  $z$  representing the vertical axis.

The  $z$ -axis control signal is multiplexed between closed and open-loop operation, as illustrated in Fig. 3. The decision index  $i$  to the multiplexer is determined by the state machine described in Section IV. During closed-loop operation, the integral controller of (3) is used. To maintain a continuous control signal,  $D_z$  needs to be pre-loaded with the right initial condition when switching modes. The difference equation associated with (3) is

$$u_i(k) = K_i e(k) + u_i(k-1), \quad (4)$$

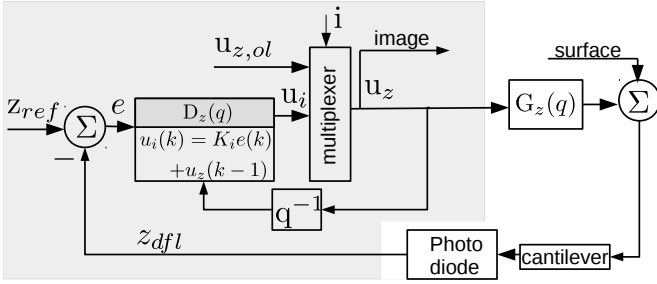


Fig. 3: Control for the  $z$ -axis is multiplexed between open and closed-loop. The shaded area represents the digital control system, while the non-shaded region is the physical system.

where  $e(k) = z_{ref} - z_{dfl}$  is the difference between the measured deflection and the reference deflection. Thus, pre-loading the integrator is easily accomplished by storing  $u(k-1) = u_{z,ol}(k-1)$  in a register.

In general, the sample surface acts as a disturbance to the  $z$ -axis control loop. When the tip is in contact with the sample, the control signal  $u_z$  is taken to represent the surface topography of the sample [1]. Due to effects such as hysteresis and creep, the control level is not absolute and simply lifting and re-engaging the tip to the same place on the surface can lead to significant differences in the control level. As discussed further in Section V, this leads to some challenges in interpreting  $\mu$ -path scan data in the absence of an absolute  $z$ -measurement.

#### IV. IMPLEMENTATION

Implementing the  $\mu$ -path CS scheme involves operating the AFM in several distinct modes, particularly in the  $z$ -direction. In the  $xy$ -direction, the system must transition from tracking a step command (in the transition to a new measurement location) to tracking a scan pattern. For our simple integral controller, this only involves changing the reference signals  $x_{ref}$  and  $y_{ref}$ .

In the  $z$ -direction, the system must transition between tip-descent, surface scanning, and tip retraction. Since our instrument does not include a  $z$ -piezo position sensor, when the tip is not engaged with the surface, the  $z$ -axis control is necessarily open-loop. Thus, the  $z$ -axis must switch between open and closed-loop operation.

Transition between, and operation in, these different modes is implemented as a simple state machine. For the  $x$  and  $y$ -axis control loops, the state machine only determines the reference signal. For the  $z$ -axis, the state machine is part of the control law itself. The state machine consists of the following stages which are executed in sequence:

- 1) **Initialization:** In this state, users have direct, manual control over the  $z$ -axis piezo, which allows them to ensure that when the rest of the process is initialized, the system is in a well defined, known state. Users also control the trigger for the state machine to enter the next state in the sequence.

- 2)  **$xy$ -move:** In the first time step of this state, we read a new  $xy$ -setpoint from a FIFO (first in, first out) buffer and set  $x_{ref}$  and  $y_{ref}$  to those values. In subsequent time steps we do not read from the FIFO buffer, but just recycle that same setpoint. The trigger to move to the next state is a detection that the  $x(k)$  and  $y(k)$  have reached a settling criterion.
- 3) **Tip engage (or  $z$ -engage):** We turn on the PI  $z$ -axis controller, which begins driving the tip towards the sample surface. Here, we use a smaller  $K_i$ , which results in somewhat slower descent and less windup while the tip is out of contact. Transition to the next state occurs when  $|e(k)|$  reaches a settling criterion.
- 4)  **$\mu$ -path scan (or  $xy$ -scan):** We initiate reading a scan trajectory from the host-to-FPGA FIFO buffer, and start logging data into the FPGA-to-host FIFO buffer. The trigger to move to the next state is that the  $xy$  trajectory we are following ends, which is determined by packing meta data into the host-to-FPGA FIFO data. This will be described more fully in Sec. IV-A.
- 5) **Tip up (or  $z$ -up):** The values of  $x_{ref}$  and  $y_{ref}$  are set to the last value of the trajectory we were following in state 4 above, and we issue a step-up command of size  $z_{up}$  to the  $z$ -axis control. We then wait  $N_{up}$  samples, before transitioning back to state 2.

Three cycles of this sequential process are illustrated by the time series in Fig. 4. Each state is represented by a different color, as indicated in the legend.

##### A. FIFO data packing

Data is transferred between the Host Computer and the FPGA in real time via a Direct Memory Access (DMA) FIFO buffer. At each time step, the FPGA control law needs to acquire the current reference trajectory (state 4) or setpoint (state 2). Similarly,  $xy$  sensor measurements,  $z$ -error deflection data, and  $z$ -axis control data all need to be transferred back to the host. The FPGA is limited to a total of three DMA FIFO buffers. Only a single scalar value can be pushed into the FIFO stack at a time (i.e., one cannot push a vector type). Thus, at each time step, we sequentially push data into the stack with the final item being a signed integer indicating the current state of the state machine, which can be visualized as:

$$FIFO = \{ \dots, \underbrace{x_1}_{\text{push scalar}}, y_1, u_{z,1}, e_1, i_1, \underbrace{x_0, y_0, u_{z,0}, e_0, i_0}_{\text{pop in multiples of 5}} \}.$$

Due to the possibility of a FIFO timeout, this is somewhat risky. On the one hand, if we wait on a piece of data too long, we violate the required sample time. On the other hand, setting a finite timeout brings the possibility of missing a piece of data and if that happens we lose all context of what the incoming data means. For smaller image sizes, these timeouts are not an issue and collecting all generated data is very useful for debugging. However, throughput becomes an issue for larger images. In that case, the timeout risk can be mostly eliminated by only transferring the data generated in state 4, which allows the host side time to

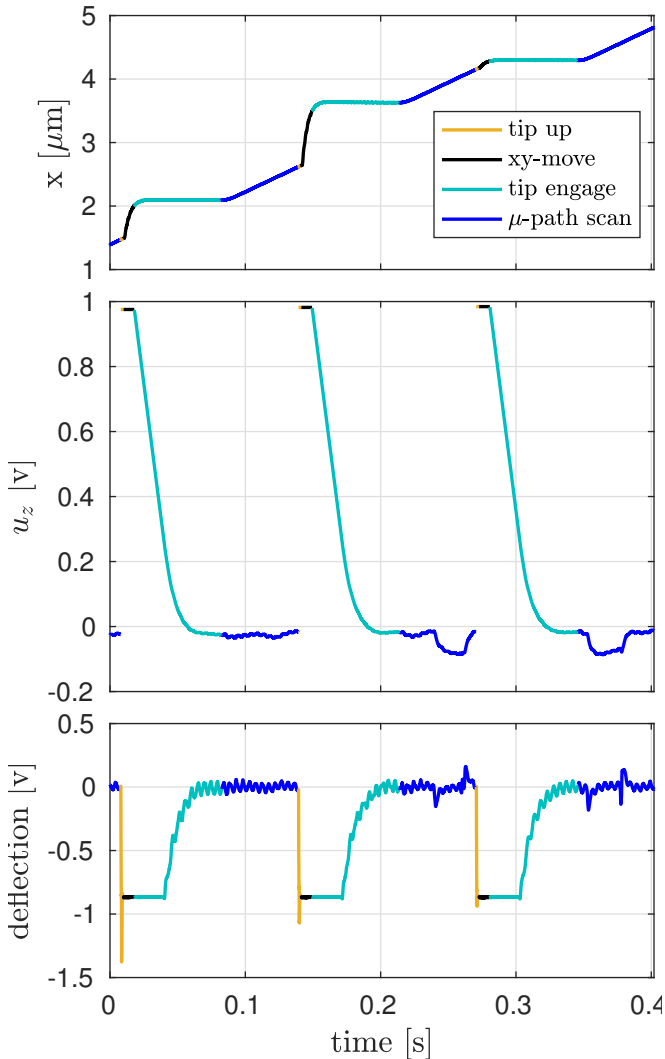


Fig. 4: Three cycles of the  $\mu$ -path scanning process. Each state of the state machine is indicated by color. The  $y$ -axis is qualitatively similar to the  $x$ -axis and so is not shown.

catch up in emptying the incoming buffer. In either case, if a timeout *does* occur, the entire imaging process enters an abort routine.

## V. COMPARISON TO RASTER SCANNING

In this study, we use an AppNano SICON-50 cantilever which is  $450 \mu\text{m}$  long, has a spring constant between 0.02 and 0.8 N/m and a resonant frequency between 5 and 25 kHz. We consider two sample gratings. The first is an UltraSharp TGZ02 linear grating which has a 3 micron pitch with 120 nm features. The second is a Ted Pella CS-20ng calibration grating. All features on the CS-20ng are 20 nm high. Although the grating has areas with several different sample patterns, here we use the area with circles on a 500 nm pitch. The Agilent 5400 does not include a  $z$ -axis height sensor. In general, this makes it impossible to determine the relative heights between CS measurements. To work around this, we make the  $\mu$ -paths  $2 \mu\text{m}$  (500 nm) long for the TGZ02 (CS-20ng) gratings, which ensures that

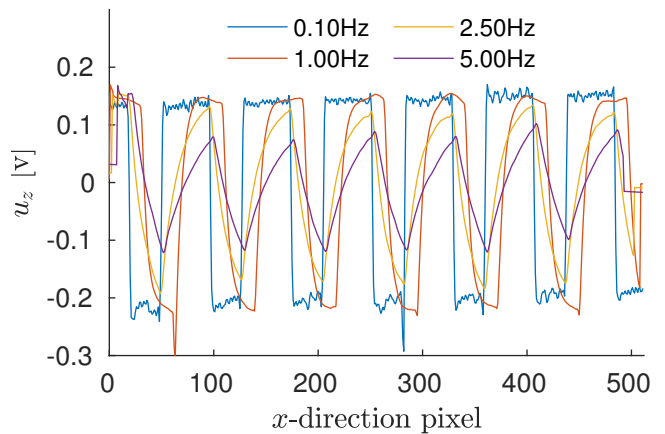


Fig. 5: A single row of the raster images in Fig. 6, which illustrates the limitation on the  $z$ -direction bandwidth.

if the scan starts on a feature, the scan must exit the feature, allowing us to register all CS measurements to a common height.

To ensure consistency with the  $\mu$ -path scans, all raster scans are taken with our own software. All scans were taken with 512 lines which produces a  $512 \times 512$  pixel image. Taking the  $u_z$  control signal to represent the sample height and discarding data from the re-trace, we divide the remaining data into  $512 \times 512$  bins based on the  $x$  and  $y$  sensor measurements. We then average the data in each bin to obtain the value of one pixel. Due to both drift in the  $z$ -axis piezo and sample tilt, this data must generally be de-trended. Though there are many procedures for such de-trending, in this paper we first de-trend each individual line. We then remove the best plane fit from the entire image. As a final step, we subtract the mean from each image, so that they can be mapped to the same color intensity in the images. Based on the sample feature sizes, we limit the range that the colormap represents which prevents one outlying data point from washing out all the images.

*TGZ02 Scans* On this grating, we performed raster scans at 0.1, 1.0, 2.5 and 5.0 Hz over a  $20 \mu\text{m}$  square area. (Note that Hz refers to line rate.) The resulting images are shown in the top row of Fig. 6. In addition, Fig. 5, shows the post-processed height data for a typical row of pixels. It is clear from these plots that 5 Hz is beyond the capability of the AFM for this sample and scanning at this rate wears and/or damages the tip to the extent that it can no longer be used for finer scans.

For the TGZ02 grating, we performed  $\mu$ -path scans with sampling densities of 3%, 10%, and 15%, with a scan velocity equivalent to a 1.0 Hz raster scan. The reconstructed images are shown in the bottom row of Fig. 6.

*CS-20ng Scans* We performed raster scans over the area with circles on a 500 nm pitch area at 0.25, 1.0, 5.0, and 10 Hz with 512 lines over a  $5 \mu\text{m}$  square. The resulting images are shown in Fig. 7 in the top row. Additionally, Fig. 8 illustrates the  $x$ -direction tracking error in the top plot. The bottom plot shows the post-processed height data for a

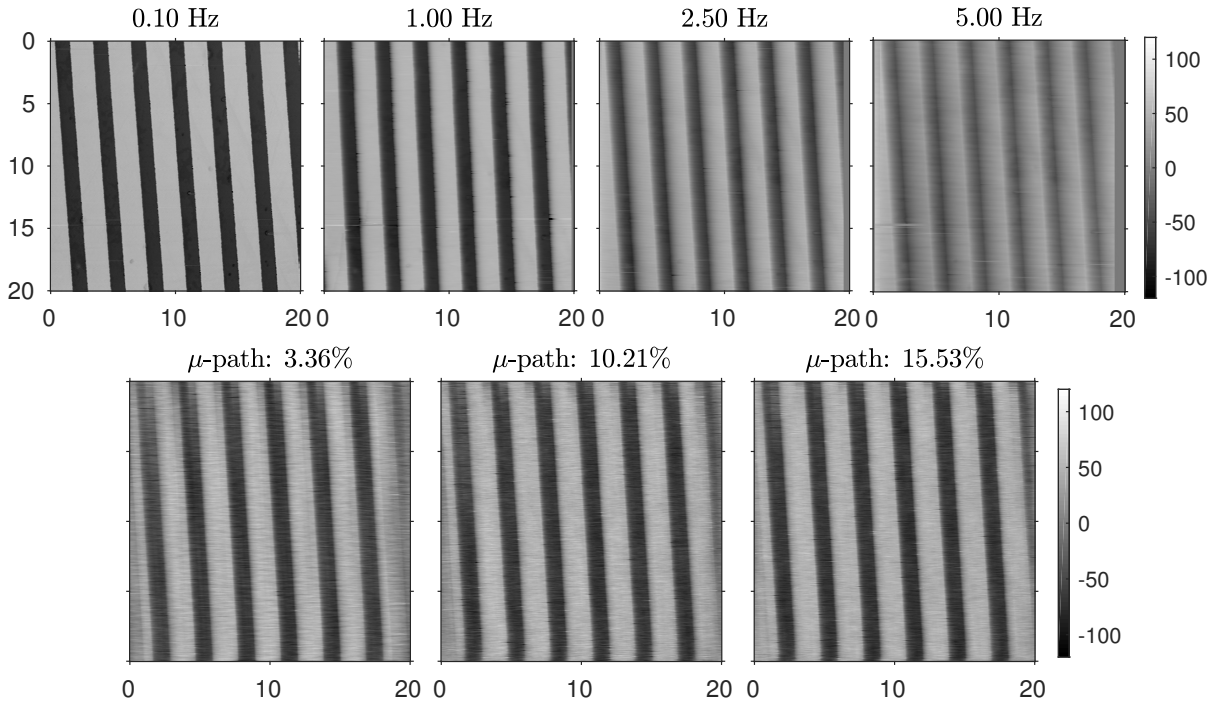


Fig. 6: Images of a 20  $\mu\text{m}$  square area of the TGZ grating. All images are  $512 \times 512$  pixels. (top row) Raster scans for scan rates of, from left to right, 0.1 Hz, 1.0 Hz, 2.5 Hz, and 5 Hz line rates. (bottom row) Reconstructions from  $\mu$ -path scans at, from left to right, nominal sampling of 3%, 10%, and 15% sampling.

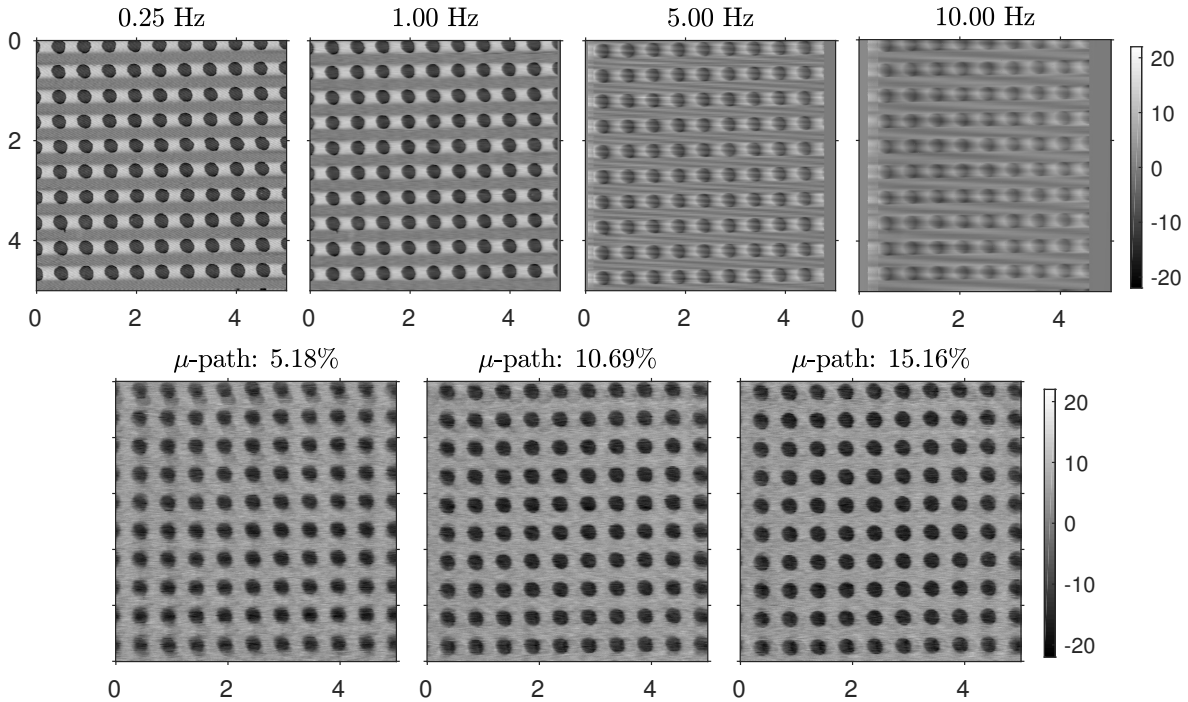


Fig. 7: Raster scans of a 5  $\mu\text{m}$  square area of the CS-2ng grating. All images are  $512 \times 512$  pixels. (top row) Raster scans for scan rates of, from left to right, 0.25 Hz, 1.0 Hz, 5 Hz, and 10 Hz. (bottom row) Reconstructions from  $\mu$ -path scans at, from left to right, nominal samplings of 5%, 10%, and 15%.

typical row of pixels. The oscillation in the 0.25 Hz cross section is likely due to vibration in our laboratory building.

When scanning much slower than 0.25 Hz on this grating, that disturbance becomes pronounced enough to be visible

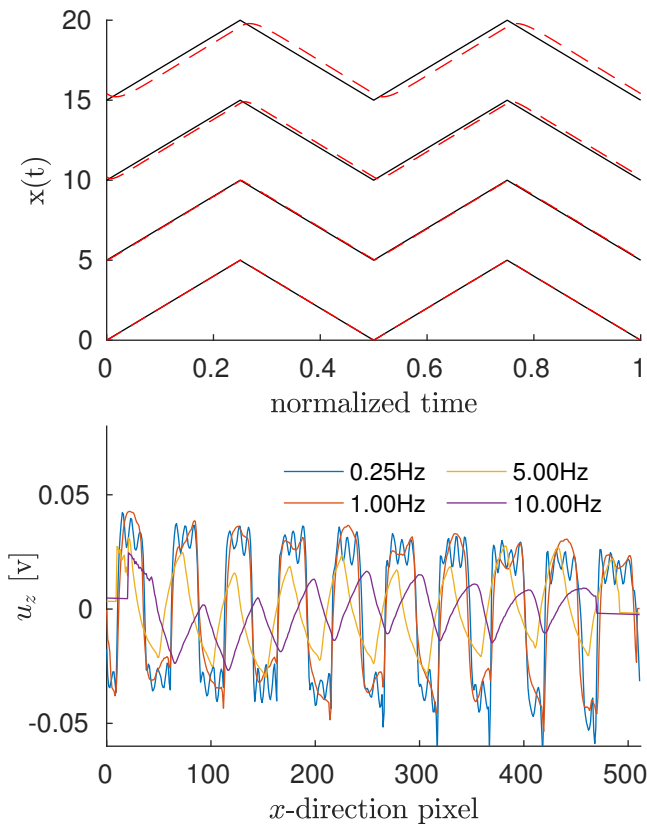


Fig. 8: Raster scanning of the CS-20ng grating. (top)  $x$ -direction tracking error for different scan frequencies with time normalized. The triangle waves for each frequency are offset for clarity with the actual trajectory shown in dashed red. From bottom to top are 0.25 Hz, 1.0 Hz, 5.0 Hz, and 10 Hz. (bottom) A single row of the raster images in Fig. 7, which illustrates the limitation on the  $z$ -direction bandwidth and the oscillatory disturbance seen at slow scan rates.

in the image. This issue is mitigated in the TGZ02 scans due to its comparatively larger feature size.

For this sample, we performed 500 nm long  $\mu$ -path scans with nominal densities of 5%, 10%, and 15% with a tip velocity equivalent to a 1.0 Hz scan. The reconstructed images are shown in the bottom row of Fig. 7.

*Discussion* From the images, it is apparent that CS does well in reconstructing the image from limited experimental data. As expected, reconstructed image quality goes up with the increase in the amount of sampling, though the reconstruction tends to lose some quality near the image edges. However, the raster scans also produce some artifacts, which is most noticeable in the scans of the CS-20ng. Specifically, the images show that the area between the holes in the  $x$ -direction is higher than the surrounding area. This shows up regardless of the sample orientation, indicating that it is a result of the raster scan or post-processing itself, not an unexpected feature of the grating.

In an attempt to provide a quantitative comparison between the different images, we use two different figures of merit. The first is the Structural Similarity Index (SSIM) [24]. The

TABLE I: Figures of merit for different raster scan rates and  $\mu$ -path scan densities for the TGZ02 and CS-20ng gratings.

	scan	SSIM	PSNR	time [sec.]
TGZ02	0.1 Hz raster	1.0	Inf	5120
	1.0 Hz raster	0.653	20.84	512
	2.5 Hz raster	0.575	20.17	204.8
	5.0 Hz raster	0.411	17.54	102.4
	15% $\mu$ -path	0.582	23.10	123.53
	10% $\mu$ -path	0.535	22.55	81.10
	3% $\mu$ -path	0.492	21.35	26.65
CS-20ng	0.25 Hz raster	1.0	Inf	2048
	1.0 Hz raster	0.305	20.81	512
	5.0 Hz raster	0.143	17.30	102.4
	10 Hz raster	0.042	13.94	51.2
	15% $\mu$ -path	0.220	18.53	104.83
	10% $\mu$ -path	0.207	19.34	73.69
	5% $\mu$ -path	0.165	19.52	35.69

second is the Peak Signal to Noise Ratio (PSNR) [18]. Both metrics compare a master image to some distorted version, and have been primarily developed by the image processing community in an effort to provide a quantitative measure of image corruption, e.g., when comparing compression algorithms. Here, for the TGZ02 and CS-20ng grating images we take the scans at 0.1 Hz and 0.25 Hz, respectively, as the master image and compute the metrics for both the faster scans as well as the reconstructed  $\mu$ -path images.

Both metrics have been used before to compare *simulations* of CS reconstruction in the context of AFM [18], [20]. We believe, however, that the numbers presented here in Table I should be interpreted with some caution as it remains somewhat of an open question of how to best compare *experimental* images from AFM. For example, it has been our experience that even comparing two raster scans over the same area and taken at the same scan rate can yield startlingly low SSIM and PSNR numbers. One of the issues causing this is that the  $xy$ -plane drifts by a small amount between images. To counteract this particular effect, the numbers in Table I were computed on a sub-slice of both the master image and the test image where one slice is shifted to provide better alignment.

From the metrics in Table I, both the 10% and 15%  $\mu$ -path scans of the TGZ02 are on par (depending on which metric you choose) with the 2.5 Hz raster while being considerably faster. For the CS-20ng all three  $\mu$ -path scans outperform the 5.0 Hz scan on both metrics while being close to the 1 Hz scan terms of PSNR and offering compelling reductions in scan time.

One of the clear advantages of  $\mu$ -path scanning is that speed increases do not solely depend on moving the tip across the sample faster. Though here we have scanned in contact mode, we believe our method should be equally applicable to tapping mode. In either case, the ability to increase imaging speed while scanning more slowly should be beneficial to imaging soft specimens.

It is both interesting and important to note that we do not achieve the reduction in imaging time which our previous estimates predicted [21]. In that work, we estimated that the tip

TABLE II: Breakdown of timing for the different  $\mu$ -path scans. Each column is a percentage of the total scan time reported in Table I.

	scan	$xy$ -move	$z$ -engage	$xy$ -scan	$z$ -up
TGZ02	15%	8.54	54.89	35.30	1.27
	10%	8.57	54.87	35.30	1.27
	3%	8.70	54.79	35.24	1.27
CS20-ng	15%	7.43	50.56	40.55	1.46
	10%	7.49	50.36	40.69	1.46
	5%	7.28	50.60	40.66	1.46

engagement should take approximately 5 times longer than the disengagement. Table II breaks down the time for each  $\mu$ -path scan. Each column is the percentage of the overall time taken in executing each state (recall Section IV). From this table, the re-engagement process takes about 40 times longer than the disengagement. The next section explores some of the limitations we encountered in the engagement process and some ideas for how they may be overcome in the future.

## VI. LIMITATION ON SPEED

The fundamental challenge with achieving speed increases through CS is the need to engage and disengage the cantilever with the sample surface for each measurement point. Table II breaks down the timing for the various  $\mu$ -path scans in terms of percentage of total time. The time to re-engage the sample takes about 50% of the total imaging time. Thus, minimizing the re-engagement time is fundamental to achieving rapid imaging with CS. Two of the main factors that control the amount of time required to engage the sample are: (1) the descent speed and (2) the starting height above the sample surface.

Both of these factors are affected by the interaction between the tip and probe which can be approximated by the Lennard-Jones model

$$F(r) = \frac{-A}{r^2} + \frac{B}{r^8}, \quad (5)$$

where  $A$  and  $B$  are parameters depending on the tip and sample properties and geometry, and  $r$  is the distance between the tip and sample [25]. A plot of (5) is shown in Fig. 9. When the tip is far away from the sample, the forces are dominated by the  $-A/r^2$  term and as the tip nears the sample surface, the interaction becomes dominated by the  $B/r^8$  term.

### A. Limitations on Approach Speed

After dis-engagement, the sample is moved to a new location in the  $xy$ -plane. The cantilever tip is then an unknown distance above the sample surface and should be sufficiently far away that  $F(r) \approx 0$ . Thus, when we begin the tip engagement and the  $z$ -axis PI controller is turned on, the deflection signal remains effectively constant until the tip begins to enter the attractive regime. Ultimately, our goal is to re-engage the sample without imparting too much force.

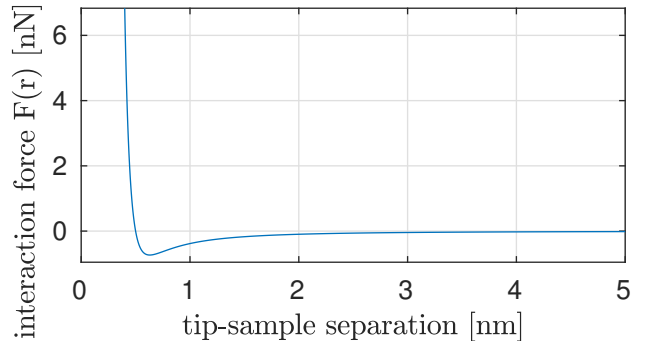


Fig. 9: Interaction force curve between the sample and the probe.

In Fig. 4, aside from residual oscillations, the tip trajectory does not really overshoot, and one might imagine that the descent could be sped up by increasing the PI gain (recall that we use a different gain here than while scanning).

In practice, increasing the gain has two negative impacts. First, it increases the amplitude of the residual oscillations, which degrades the resulting image. The second is that on occasion, the larger oscillations will refuse to decay (exhibiting a limit cycle like behavior) or decay very slowly.

In this work, we address these issues first by limiting the gain used during the engagement, though unfortunately, this increases the overall scanning time. Second, we take advantage of the observation that starting the  $xy$ -scan will collapse the oscillations when they refuse to decay. Thus, in the images generated above, we set an upper limit on how many sample periods we are willing to wait for the  $z$ -axis to settle before starting the scan. This keeps the imaging process moving along, but unfortunately can lead to undesirable transients at the beginning of the  $xy$ -scan.

### B. Starting Height Above the Sample

Ideally, we would lift the tip just high enough above the sample to prevent a tip-sample collision while we execute the  $xy$ -move and in prior work this was one of the assumptions made in calculating our timing estimates [17], [21]. Unfortunately, the interaction forces between the tip and sample keeps the tip clamped to the sample surface until the cantilever is bent far enough that the spring force exceeds the tip-sample attractive force. This means that the height of disengagement is farther from the sample than the engagement point [26]. Thus, it is insufficient, *e.g.*, to step the  $z$ -axis up by say 25 nm (for the CS20-ng). Indeed, we found that we needed to step up by approximately 350 nm to fully break contact with the CS-20ng. This is a major contributor to the re-engagement time. One possible way to overcome this would be to step up by a large amount to break contact and then quickly step down some fraction of that while performing the  $xy$  transition.

## VII. CONCLUSIONS AND FUTURE WORK

In this work we have given an experimental demonstration of ideas we have previously pursued through simulation studies [17], [18], [21]. Our  $\mu$ -path based sub-sampling produced

quality reconstructed images, and, while we did not see the full speed increase in imaging time we previously estimated, significant gains over raster imaging were demonstrated. The experiments also revealed that reduced improvement is largely due to complexities in re-engaging the sample.

It is clear from the discussion in Sec. VI and Figs. 5 and 8 that, at least in these results, the limiting factor for both scanning methods is primarily in the  $z$ -axis. Although the frequency response of the piezo tube in our AFM does not begin to rolloff until about 2 kHz, there is a prominent, lightly damped pole-zero pair at about 215 Hz. In raster scanning, this mode limits the achievable bandwidth using PI control and thus limits the scan rate. Similarly, it is this mode which gets excited during the descent in  $\mu$ -path scanning, frustrating our attempts to descend faster.

The sample engagement problem has not received much attention in the literature, particularly when considering how to do so as rapidly as possible. Thus, an interesting area for future work is to study the dynamics during this phase and develop control schemes to account for them. This should allow a much more complete characterization of the fundamental limitations in our  $\mu$ -path approach and permit a more complete comparison to the known limitations on raster scanning [27] as it relates to  $z$ -axis bandwidth.

#### REFERENCES

- [1] D. Y. Abramovitch, S. B. Andersson, L. Y. Pao, and G. Schitter, "A tutorial on the mechanisms, dynamics, and control of atomic force microscopes," in *Proc. American Control Conf.*, July 2007, pp. 3488–3502.
- [2] G. Schitter, K. J. Astrom, B. E. DeMartini, P. J. Thurner, K. L. Turner, and P. K. Hansma, "Design and modeling of a high-speed AFM-scanner," *IEEE Trans. Control Systems Tech.*, vol. 15, no. 5, pp. 906–915, Sep. 2007.
- [3] B. J. Kenton and K. K. Leang, "Design and control of a three-axis serial-kinematic high-bandwidth nanopositioner," *IEEE/ASME Trans. Mechatronics*, vol. 17, no. 2, pp. 356–369, April 2012.
- [4] I. A. Mahmood and S. O. R. Moheimani, "Fast spiral-scan atomic force microscopy," *Nanotechnology*, vol. 20, no. 36, p. 365503, 2009.
- [5] T. Tuma, J. Lygeros, V. Kartik, A. Sebastian, and A. Pantazi, "High-speed multiresolution scanning probe microscopy based on Lissajous scan trajectories," *Nanotechnology*, vol. 23, no. 18, p. 185501, Apr. 2012.
- [6] M. S. Rana, H. R. Pota, and I. R. Petersen, "Spiral scanning with improved control for faster imaging of AFM," *IEEE Trans. Nanotech.*, vol. 13, no. 3, pp. 541–550, May 2014.
- [7] A. Fleming, B. Kenton, and K. Leang, "Bridging the gap between conventional and video-speed scanning probe microscopes," *Ultramicroscopy*, vol. 110, no. 9, pp. 1205 – 1214, 2010.
- [8] J. Butterworth, L. Y. Pao, and D. Abramovitch, "Dual-adaptive feedforward control for raster tracking with applications to AFMs," in *Proc. IEEE Int. Conf. Control Applications*, Sep. 2011, pp. 1081–1087.
- [9] Y. Li and J. Bechhoefer, "Feedforward control of a closed-loop piezoelectric translation stage for atomic force microscope," *Review of Scientific Instruments*, vol. 78, no. 1, p. 013702, 2007.
- [10] B. Bhikkaji and S. O. R. Moheimani, "Integral resonant control of a piezoelectric tube actuator for fast nanoscale positioning," *IEEE/ASME Trans. Mechatronics*, vol. 13, no. 5, pp. 530–537, Oct. 2008.
- [11] K. K. Leang, Q. Zou, and S. Devasia, "Feedforward control of piezoactuators in atomic force microscope systems," *IEEE Control Systems Magazine*, vol. 29, no. 1, pp. 70–82, Feb. 2009.
- [12] Y. K. Yong and S. O. R. Moheimani, "Collocated  $z$ -axis control of a high-speed nanopositioner for video-rate atomic force microscopy," *IEEE Trans. Nanotech.*, vol. 14, no. 2, pp. 338–345, Mar. 2015.
- [13] G. Schitter and M. J. Rost, "Scanning probe microscopy at video-rate," *Materials Today*, vol. 11, pp. 40 – 48, 2008.
- [14] P. Huang and S. B. Andersson, "Note: Fast imaging of DNA in atomic force microscopy enabled by a local raster scan algorithm," *Review of Scientific Instruments*, vol. 85, no. 6, p. 066101, June 2014.
- [15] B. Hartman and S. B. Andersson, "Feature tracking for high-speed AFM: Experimental demonstration," in *Proc. American Control Conf.*, May 2017, pp. 773–778.
- [16] B. Song, N. Xi, R. Yang, K. W. C. Lai, and C. Qu, "Video rate atomic force microscopy (AFM) imaging using compressive sensing," in *Proc. IEEE Int. Conf. Nanotech.*, Aug. 2011, pp. 1056–1059.
- [17] S. Andersson and L. Pao, "Non-raster sampling in atomic force microscopy: A compressed sensing approach," in *Proc. American Control Conf.*, June 2012, pp. 2485–2490.
- [18] Y. Luo and S. B. Andersson, "A comparison of reconstruction methods for undersampled atomic force microscopy images," *Nanotechnology*, vol. 26, no. 50, p. 505703, 2015.
- [19] A. Chen, A. L. Bertozzi, P. D. Ashby, P. Getreuer, and Y. Lou, "Enhancement and recovery in atomic force microscopy images," in *Excursions in Harmonic Analysis, Vol. 2*. Boston: Birkhäuser Boston, Nov. 2012, pp. 311–332.
- [20] C. S. Oxvig, T. Arildsen, and T. Larsen, "Structure assisted compressed sensing reconstruction of undersampled AFM images," *Ultramicroscopy*, vol. 172, pp. 1–9, Jan. 2017.
- [21] B. D. Maxwell and S. B. Andersson, "A compressed sensing measurement matrix for atomic force microscopy," in *Proc. American Control Conf.*, June 2014, pp. 1631–1636.
- [22] A. Y. Carmi, *Compressive System Identification*. Berlin, Heidelberg: Springer Berlin Heidelberg, 2014, pp. 281–324.
- [23] Y. Luo and S. B. Andersson, "A fast image reconstruction algorithm for compressed sensing-based atomic force microscopy," in *Proc. American Control Conf.*, July 2015, pp. 3503–3508.
- [24] Z. Wang, A. C. Bovik, H. R. Sheikh, and E. P. Simoncelli, "Image quality assessment: from error visibility to structural similarity," *IEEE Trans. Image Processing*, vol. 13, no. 4, pp. 600–612, April 2004.
- [25] G. Schitter, P. Menold, H. F. Knapp, F. Allgwer, and A. Stemmer, "High performance feedback for fast scanning atomic force microscopes," *Review of Scientific Instruments*, vol. 72, no. 8, pp. 3320–3327, 2001.
- [26] S. M. Salapaka and M. V. Salapaka, "Scanning probe microscopy," *IEEE Control Systems Magazine*, vol. 28, no. 2, pp. 65–83, April 2008.
- [27] Y. R. Teo, Y. K. Yong, and A. J. Fleming, "A comparison of scanning methods and the vertical control implications for scanning probe microscopy," *Asian Journal of Control*, vol. 19, no. 2, pp. 1–15, 2017.